THE BALTIC JOURNAL
OF ROAD AND BRIDGE ENGINEERING
2026/21(2)

ISSN 1822-427X/eISSN 1822-4288
2026 Volume 21 Issue 2: 1–30
https://doi.org/10.7250/bjrbe.2026-21.676

CASE STUDY OF MECHANICAL PERFORMANCE OF KILOMETER LEVEL CABLE-STAYED BRIDGES WITH STEEL-CONCRETE COMPOSITE DECK

TINGTING MA[*,1], SHISHOU ZHANG[1], MEITAO SHANG[2]

[1]*College of Ocean Science and Engineering, Shanghai Maritime University, Shanghai, China*

[2]*CCCC Shanghai Harbor Engineering Design & Research Institute Co., Ltd., Shanghai, China*

Received 22 November 2025; accepted 21 May 2026

Abstract. In view of the shortcomings of large dead-weight and limited spanning capacity for traditional composite girders and the fatigue failure and pavement deteriorations for steel girders, composite girders with lightweight composite deck emerged as good alternatives. Thus, trial design schemes of long-span cable-stayed bridges with steel-NC (normal concrete) and steel-UHPC (ultra-high performance concrete) composite decks were proposed under different span conditions. The static performance and technical feasibility of the designed bridges and the influence of structural parameters of main girder on different static effects were analysed, based on which, the determinative static effects and their variation with span length were investigated. The results show that the designed NC-slab schemes with main spans no more than 900 m can meet the requirements of static strength, stiffness and stability, while the 1000 m NC-slab scheme cannot meet the compressive strength requirements of the concrete slab. The UHPC-slab schemes meet the static requirements even when the main span reaches 1100 m, and the most unfavourable static effect turns to be the maximum compressive stress of steel girders. The main structural parameters of the main girder that most affect the unfavourable static effects include the main girder height and the

* Corresponding author. E-mail: ttma@shmtu.edu.cn

Tingting MA (ORCID ID 0000-0001-7803-7709)
Shishou ZHANG (ORCID ID 0009-0009-4786-3851)
Meitao SHANG (ORCID ID 0009-0000-9014-5964)

thickness of the lower flange steel plate. Using UHPC-slab instead of NC-slab improves the spanning capacity of cable-stayed bridges by approximately 25%, close to the reduction rate of the dead-weight of main girder.

Keywords: cable-stayed bridge, composite open deck section, normal concrete, ultra-high performance concrete, static performance, spanning capacity, trial design.

Introduction

Cable-stayed bridges developed rapidly in the last half century due to their good mechanical properties, large spanning capacities, and good economic performances. Long-span cable-stayed bridges with a main span exceeding 1000 m have been built, such as the Sutong Bridge in China with a main span of 1088 m and the Russky Island Bridge in Russia with a main span of 1104 m (Syrkov & Krutikov, 2014). The Changtai Yangtze River Bridge in China, having a main-span of 1176 m, breaks the world's span record of cable-stayed bridges. Meanwhile, much effort has been devoted to investigations on span limitations of cable-stayed bridges (e.g., Nagai et al., 2004; Zhao et al., 2019; Yang et al., 2020). For long-span cable-stayed bridges, steel girders with orthotropic steel bridge decks are mostly used, which have advantages of large bearing capacity, light dead-weight and convenient construction. However, the excessive stress amplitudes in the steel deck and welding seams due to insufficient deck stiffness, as well as the inappropriate details both make the conventional orthotropic steel deck system prone to fatigue cracks (Wolchuk, 1990; Shao et al., 2013). Additionally, the flexible orthotropic steel deck makes the pavement damage problem become prominent, and thus shortens the service life of pavements (Kim et al., 2014). Based on the popular concept of "high-performance structural engineering", durability and life-cycle economic performance have become important factors restricting the further application and development of orthotropic steel decks in long-span cable-stayed bridges.

To solve the problems of orthotropic steel bridge decks, composite girders with concrete deck can be used. However, the heavy self-weight of traditional composite girders limits the breakthrough of the main-span length of composite girder cable-stayed bridges, which in turn limits their wider application. At present, the largest composite girder cable-stayed bridge with concrete deck is the Gordie Howe International Bridge with a main span of 853 m (Martin et al., 2023). As a result, the lightweight steel-concrete composite deck system emerged as a new alternative (e.g., Walter et al., 2007; Shao et al., 2018; Chen et al., 2019). The significant advantage of this deck system over the orthotropic steel deck system lies in the fact that it enhances the deck stiffness, thus effectively reducing the stresses in both the deck plate and the connection between the deck plate and the longitudinal ribs under wheel loads (Shao et al., 2013). Meanwhile, compared with concrete decks in

conventional composite girders, the lighter self-weight of the composite deck makes it possible to further enhance the span capacity of composite-girder cable-stayed bridges.

As an innovative and advantageous bridge deck system, lightweight composite deck has been increasingly applied in engineering practice. The Dongting Lake Suspension Bridge in China with a main span of 1480 m adopts a plate-truss composite stiffening girder with composite deck (Li et al., 2022). The Second Hanjiang River Bridge in China, a single-tower cable-stayed bridge with a main span of 310 m, has an 80 mm-thick high-performance concrete slab between the orthotropic steel deck and the pavement. Steel-concrete composite decks were also used in renovation projects of conventional orthotropic steel decks, such as the deck renovations of a single-pylon cable-stayed bridge (Shao & Cao, 2018) and a continuous truss bridge (Shao et al., 2019) in China. Currently, the engineering application of composite deck in cable-stayed bridges is mainly limited to small-span cable-stayed bridges. The completion of the partially earth-anchored Danjiangkou Reservoir Bridge with a main span of 760 m in China in 2023 signifies the first successful application of composite decks in long-span cable-stayed bridges (Liao et al., 2023). However, in engineering practice, a certain gap remains between the spanning capacity of composite girder cable-stayed bridges and that of steel girder cable-stayed bridges. Although the current engineering practice of lightweight composite decks in long-span cable-stayed bridges is limited, with the application of new materials such as ultra-high performance concrete (UHPC) (e.g., Al-Ramahee et al., 2017; Shao et al., 2018) and the development of different lightweight composite deck structures (e.g., Kim & Jeong, 2010; Su et al., 2019; Liu et al., 2019), composite decks present good application prospects in long-span cable-stayed bridges. A few trial design studies on kilometre level cable-stayed bridges using composite decks were carried out. For instance, Yao and Shao (2018) preliminarily verified the feasibility of a 1100 m-main-span cable-stayed bridge with lightweight steel-UHPC composite deck from the viewpoints of static performance, dynamic characteristics and economic performance, and the main girder was designed with a box section and a PK section. However, traditional composite cable-stayed bridges usually adopt open-section composite girders with superior force transmission and economic performance. The mechanical performance of kilometre level open-section composite-girder cable-stayed bridges with steel-concrete composite deck remains to be explored.

Parametric analysis is a useful way to investigate the mechanical performance of novel structural systems, and has been widely employed to improve the structural performance of cable-stayed bridges. For instance, a detailed parametric analysis was conducted by Zhao et al. (2019) for steel girder cable-stayed bridges to explore the relationship between the span limit and key structural parameters, including the height-to-span ratio, cable strength, cable spacing, and load weight on the girder.

Arellano et al. (2019) performed a parametric analysis to evaluate the influence of pier, pylon, and deck stiffness on the mechanical behaviour of multi-span cable-stayed bridges under alternate live loads. More recently, Zhang et al. (2024) carried out a parametric analysis for a three-tower cable-stayed bridge with main spans of 1400 m to determine a favourable structural scheme with enhanced aerostatic and aerodynamic stability, considering parameters such as the tower height-to-span ratio and girder depth. Jiao et al. (2024) analysed the impact of different structural system types (different number of towers and girder-pier connection forms in the longitudinal direction) on the seismic fragility of a multi-tower cable-stayed bridge. These studies provide valuable insights into the parameter sensitivity of cable-stayed bridges. However, parametric investigations focusing on long-span cable-stayed bridges with open-section composite girders and steel-concrete composite decks remain limited.

In this study, five sets of trial design schemes for long-span open-section composite-girder cable-stayed bridges (abbreviated as OCCBs) with steel-concrete composite deck (abbreviated as SCD) were proposed. Three-dimensional finite element (FE) models were established for each design scheme using the TDV RM Bridge computer program. The mechanical performance and technical feasibility of each scheme was analysed, and the determinative static effect was discussed. Furthermore, parametric analysis was carried out to investigate the sensitivity of structural static performance to primary structural parameters of the main girder. Finally, the variation of the most unfavourable static effects of the proposed OCCBs with main span length was discussed. This study contributes to improving the competitiveness of composite girder cable-stayed bridges in a larger span range and providing more feasible structural systems for the design of future long-span cable-stayed bridges.

1. Overview of trial design schemes

1.1. Main design conditions

The main design conditions for the trial design of OCCBs with SCD are summarised in Table 1, including the design loads, load combinations and material properties. As shown in Table 1, the design loads mainly include dead load, vehicle load, wind load, temperature load, settlement effect, and shrinkage and creep effect. The dead load is composed of Phase I and Phase II dead load. The Phase I dead load was calculated according to the actual section area of the main girder, taking into account the diaphragms and other components, and the Phase II dead load of 90 kN/m accounts for the pavement, handrails, curbs, and attachments, etc. The design wind speed at a height of 10 m (V_{s10}) was taken as 41.12 m/s with reference

to the design parameters for the Xihoumen Sea-Crossing Suspension Bridge in China to simulate an offshore wind environment, and the A-type power law wind profile with a surface roughness coefficient of 0.12 was assumed. The reference height of the main girder was set to 65 m for this case study, and thus the reference wind speed at the main girder height is 51.5 m/s. The drag force coefficients of the main girder and stay cables were assumed to be 1.3 and 0.8, respectively, according to the Chinese wind-resistant design specification for highway bridges (JTG/T 3360-01–2018, 2018). For the towers, the drag force coefficient was determined according to the actual section shape of the tower column at different heights. The temperature load includes the effects of an overall temperature difference of ±20 °C and a gradient temperature difference of ±10 °C at the bridge deck. The foundation settlement effect was considered by selecting the most unfavourable combination of a 10 cm settlement of each tower and a 5 cm settlement of each pier. The effect of shrinkage and creep was calculated according to the Chinese specifications for design of highway reinforced concrete bridges (JTG 3362–2018, 2018), and the initial loading age of concrete slab was set to 270 days.

The fundamental combination of actions was considered in this study, including the operational load combinations and extreme wind load combinations of bridge under the newly completed state and the state 10 years after completion. The details of these four different load combinations are shown in Table 1. Compared with the newly completed state, the main difference in load combinations for the bridge completed for 10 years is the consideration of the shrinkage and creep effect of concrete. The selection of a 10-year extension period for the calculation of the shrinkage and creep effect is mainly due to the small increase in the shrinkage strain and creep coefficient of concrete 10 years after the completion of the bridge (JTG 3362–2018, 2018). Additionally, it should be explained that different load cases for the live load in the deck were considered to obtain the most unfavourable effects.

The materials used for the trial design mainly include Q420qE steel for steel girders and steel deck plates, normal concrete with material grade C60 (NC-C60) and UHPC for deck slabs of different main span schemes, NC-C50 for bridge towers, and high-strength steel wires for stay cables. The design strength of different materials is shown in Table 1, where f'_{d} and f_{d} respectively represent the design compressive and tensile strength of steel, f_{cd} and f_{td} respectively represent the design compressive and tensile strength of concrete, f'_{sd} and f_{sd} are respectively the design compressive and tensile strength of HRB500 reinforcing bars, and E_{c} and E_{s} denote the elastic moduli of concrete and steel, respectively. The material properties in Table 1 except for the UHPC are taken from relevant design specifications (JTG 3362-2018, 2018; JTG D64-2015, 2015). The material mechanical properties of UHPC mainly refer to the test results of Shao et al. (2022).

Table 1. Main design conditions

Design conditions		Descriptions
Design loads	Dead load	Phase I: Self-weight of main girder, taking into account the diaphragms and other components Phase II: 90 kN/m
	Vehicle load	Highway – Class I, with a total of 8 lanes
	Wind load	Operational wind load under operational wind speed of 25 m/s Extreme wind load under reference wind speed of 51.5 m/s
	Temperature load	Overall temperature difference: ±20 °C (main girder) Gradient temperature difference: ±10 °C (concrete slab)
	Settlement	Towers: 10 cm; Piers: 5 cm
	Shrinkage and creep	Initial loading age of concrete slab: 270 days
Load combinations	Comb. 1	Dead load + Settlement + Temperature load + Operational wind load + Vehicle load + Braking force
	Comb. 2	Dead load + Settlement + Temperature load + Operational wind load + Vehicle load + Braking force + Shrinkage and creep
	Comb. 3	Dead load + Settlement + Temperature load + Extreme wind load
	Comb. 4	Dead load + Settlement + Temperature load + Extreme wind load + Shrinkage and creep
Material properties	Steel girder	Q420qE: $f_d = f'_d = 305$ MPa, $E_s = 2.06 \times 10^5$ MPa
	Reinforced concrete slab	NC-C60: $f_{cd} = 26.5$ MPa, $f_{td} = 1.96$ MPa, $E_c = 3.6 \times 10^4$ MPa UHPC: $f_{cd} = 97.7$ MPa, $f_{td} = 8.0$ MPa, $E_c = 4.85 \times 10^4$ MPa HRB500: $f_{sd} = 415$ MPa, $f'_{sd} = 400$ MPa, $E_s = 2.0 \times 10^5$ MPa
	Towers	NC-C50: $f_{cd} = 22.4$ MPa, $f_{td} = 1.83$ MPa, $E_c = 3.45 \times 10^4$ MPa
	Stay cables	PES: $f_d = 1005$ MPa, $E_s = 1.95 \times 10^5$ MPa

1.2. Details of trial design schemes

Under the aforementioned design conditions, trial design schemes of OCCBs with main spans of 800 m, 900 m, 1000 m and 1100 m were proposed. The primary design parameters of the designed bridges are shown in Table 2. Each design scheme was arranged as a 5-span continuous symmetrical structure with two diamond-shaped towers, two side piers (SPs) and two auxiliary piers (APs). The side-to-main span ratio was set to 0.45 for each design scheme, which is within the commonly used side-to-main span ratio range of 0.4 to 0.5 for composite cable-stayed bridges.

The open-section composite girder consisting of a steel-concrete composite deck system and double steel box girders was selected for each trial design

scheme considering the advantages of simple longitudinal and transverse beam lattice system, clear and efficient force transmission, and satisfactory economic performance, as shown in Figure 1. The thickness of the steel deck plates is 8 mm. Different concrete materials were adopted for concrete slabs for investigation of the impact of concrete material on structural mechanical performance, including the NC-C60 for the 800 m, 900 m and 1000 m main-span schemes, and the UHPC for the 1000 m and 1100 m main-span schemes. The standard thickness of the concrete slab is 14 cm for the NC slab and 8 cm for the UHPC slab. Considering the large axial force and wind-induced bending moment in the main girder at the tower location and the unfavourable forces at the side spans, the thickness of the concrete slab at relevant locations was increased. The main plates of the steel box girders, such as the lower flange plates, were also designed with variable thickness according to the internal force distribution. The concrete slabs were designed to be integrally prefabricated with the steel girders to form composite girder segments, and the integral hoisting construction of the composite girder segments was assumed in this study.

Table 2. Primary structural parameters for trial design schemes of cable-stayed bridges

Design parameters	Main-span length			
	800 m	900 m	1000 m	1100 m
Span layout, m	132+228+800 +228+132	144+261+900 +261+144	165+285+1000 +285+165	177+318+1100 +318+177
Tower height, m	222	242	262	282
Main girder width, m	39.5	39.5	39.5	39.5
Main girder height, m	4.0	4.0	4.0	4.0
Thickness of concrete slab, cm	14~18 (C60)	14~18 (C60)	14~18 (C60) 8~12 (UHPC)	8~12 (UHPC)
Thickness of steel deck plate, mm	8.0	8.0	8.0	8.0
Thickness of lower flange steel plate, mm	17~41	31~42	30~44 (C60) 27~40 (UHPC)	31~43
Number of stay cables/pair	116	132	164	180
Cable distance (mid-span), m	13.5	13.5	12.0	12.0
Cable distance (side-span), m	10.5, 13.5	10.5, 13.5	9.5, 12.0	9.5, 12.0
Elastic stiffness, kN/m	20 000	20 000	50 000	50 000

The bridge towers of each design scheme are made of reinforced concrete and designed with a diamond shape, as shown in Figure 2. The stay cables are made of

galvanized parallel steel wires, and Figure 3 shows the cross-sectional area of each stay cable for different span schemes. A semi-floating system was selected for each design scheme, and a pair of elastic connections was set between the main girder and the crossbeam of each tower to limit the longitudinal drift displacement of the main girder. The elastic stiffness of individual longitudinal elastic connection for each design scheme is shown in Table 2.

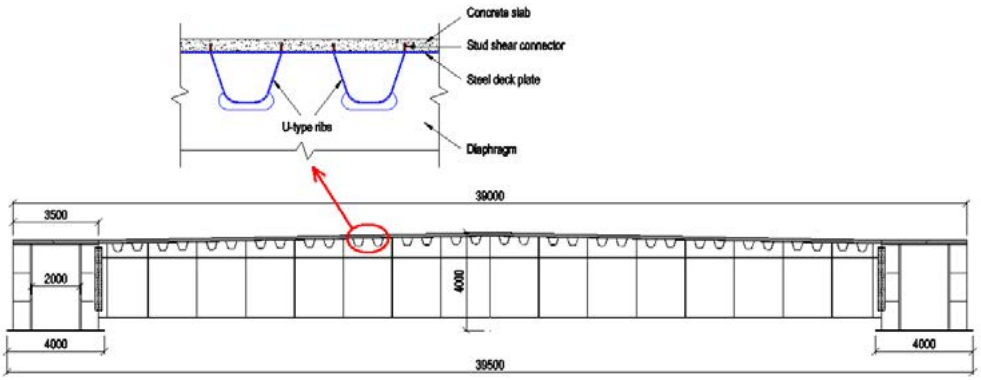

Figure 1. Cross section of main girder (Unit: mm)

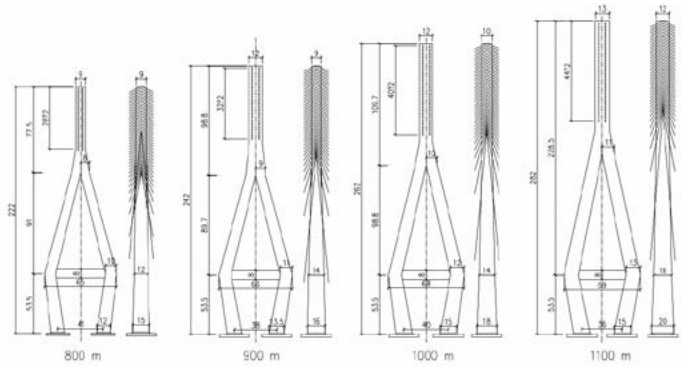

Figure 2. Layout of bridge towers (Unit: m)

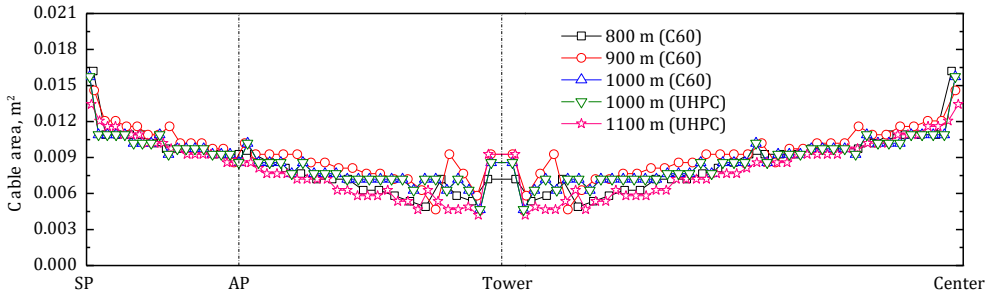

Figure 3. Cross-sectional area of stay cables

2. Mechanical performance of trial design schemes

2.1. FE modelling

The FE models of the proposed cable-stayed bridges were developed using the software TDV RM Bridge. Figure 4 shows the FE model of the trial design scheme with a main span of 1000 m as an example. The composite girder was modelled using three-dimensional (3-D) elastic beam elements with six degrees of freedom at each node, a commonly used modelling method in previous studies (e.g., Yang et al., 2017; Wang et al., 2023). The composite deck sections for the beam elements were generated by separately creating corresponding geometric sections of the concrete slab, the steel deck plate and the steel box girders, and the sectional constants can be automatically calculated in the TDV RM Bridge program based on the input geometric parameters and material properties of each component of the cross-section. The reinforcement in the concrete slab was not simulated in the FE model for simplicity. The towers and piers were also modelled by 3-D elastic beam elements. The element size of the main girder is around 3.5 m, with the girder segment between two adjacent cables divided into three beam elements. For the towers, the beam element length ranges approximately from 2.0 m to 3.5 m. The beam element sizes were determined based on a mesh effect analysis. The stay cables were simulated by 3-D tension-only elastic bar elements, and the elastic moduli of the stay cables were modified using the Ernst formula to consider the sag effect (Yang et al., 2017; Wang et al., 2023). This simplified cable model has been validated in obtaining reliable static load effects even in a cable-stayed bridge with a main span of 1316 m (Wen & Zhou, 2022). In the FE models, the linear elastic

material constitutive models were adopted and the material properties are shown in Table 1.

Based on the designed semi-floating system, the longitudinal elastic connections between the main girder and the towers were modelled by spring elements, and the transverse connections were simulated by coupling constraints. Coupling constraints were also used between the main girder and bridge piers to realize the coupling of their vertical and lateral translational degrees of freedom, as well as torsional degrees of freedom about the bridge axis. The towers and piers were fully constrained at the base. The Phase II dead load was applied to the girder spine in the form of line load. The influence of geometric nonlinear factors such as beam-column effect and large deformation effects was considered in the FE static analyses.

Figure 4. Finite element model of 1000 m-main-span cable-stayed bridge

2.2. Reasonable finished state of bridge

Determination of the reasonable finished state of bridge, which mainly depends on the optimisation of cable forces, is a key issue in the design of cable-stayed bridges, and is also an important basis for subsequent static performance analyses. The reasonable finished state of a cable-stayed bridge includes requirements in both the structural internal force and the alignment of the bridge. In this study, the widely used influence matrix method (Xiao et al., 2001) was adopted to optimise cable forces, and the reasonable finished state of the designed cable-stayed bridges should meet the following specific requirements: (1) The girder is basically flat and the pylons are straight prior to the applications of live loads, i.e., the displacement of the main girder and towers under the action of dead load are kept within corresponding "feasible ranges" (0.03 cm for the side span girder, 0.001 m for the centre span girder and 0.001 m for the towers); (2) The cable force generally increases uniformly as

the cable length increases, and there is no tension relaxation for each cable; (3) The reaction force at the top of both the side piers and the auxiliary piers has a certain pressure reserve, and no tensile reaction force occurs under the action of various live loads.

Based on the above-mentioned principles for cable force optimisation, the reasonable internal force of stay cables for the reasonable finished state of bridge was determined in an iterative way. The cable force distributions of different trial design schemes are shown in Figure 5. In view of the symmetrical arrangement of the designed cable-stayed bridges, results of only half span of the bridges were given in corresponding figures. It can be seen that the cable force generally increases uniformly with the increase of the cable length, and only the cable force in the local area near the bridge tower changes abruptly. Correspondingly, the vertical displacement of the main girder and the longitudinal displacement of the tower in the finished state of different span schemes are controlled within their predefined feasible ranges.

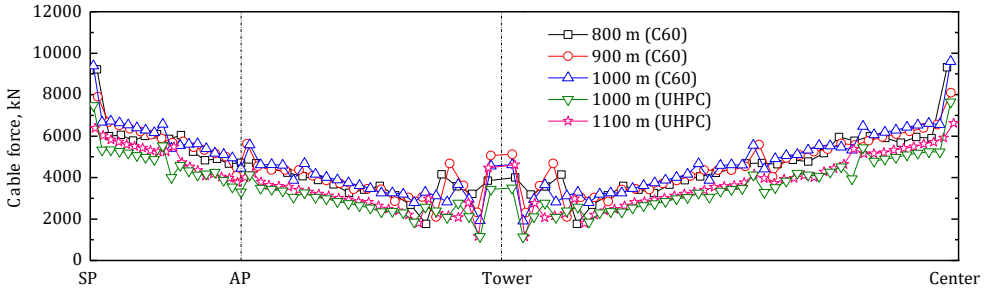

Figure 5. Distributions of cable force in finished state of bridge

Figure 6 depicts the distributions of the axial force and the bending moment of the main girders in the finished state of bridge. It can be seen that the use of thin UHPC slab significantly reduces the axial force of the main girder, and a reduction rate of 23.7% is observed for the 1000 m-main-span scheme. The distributions of the bending moment are relatively uniform, especially in the middle span. The maximum bending moment occurs near the bridge towers and the auxiliary piers. It needs to be explained that the relatively large bending moment near the auxiliary piers can be further reduced by adjusting the weight load at side spans.

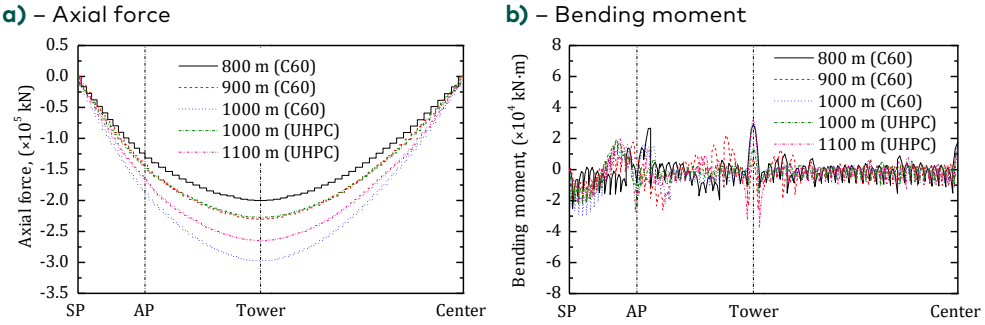

Figure 6. Internal forces of main girders in finished state of bridge

2.3. Strength analysis

1. Key stress points

In order to obtain the most unfavourable stress response on cross-sections of the composite girders under different load combinations, several key stress points were selected on deck section for stress extraction. The key stress points are shown in Figure 7, in which DC01 and DC02 are unfavourable stress points on the concrete slab, and GS01 and GS02 are stress points at the top and bottom edges of the steel girder, respectively. The stress response at the specified stress points can be directly extracted from the TDV RM Bridge program.

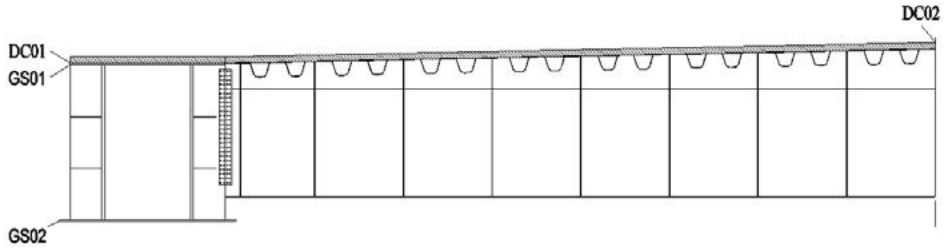

Figure 7. Layout of key stress points on half of bridge deck section

2. Stress distribution

By extracting the stress envelope of each stress point under different load combinations, the stress envelope of steel girders and concrete slabs along the full span can be obtained. Figures 8 and 9 respectively show the longitudinal normal

stress envelopes of the steel girders and concrete slabs for each trial design scheme under the four load combinations described in Section 1.1 The variation of the most unfavourable stresses with the main span length is shown in Figure 10, in which σ_{sc} and σ_{st} respectively represent the maximum compressive and tensile stresses of the steel girders, while σ_{cc} and σ_{ct} correspond to those of the concrete.

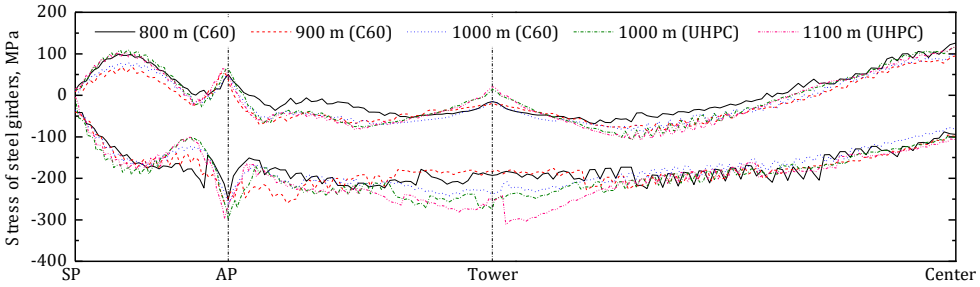

Figure 8. Longitudinal normal stress envelopes of steel girders

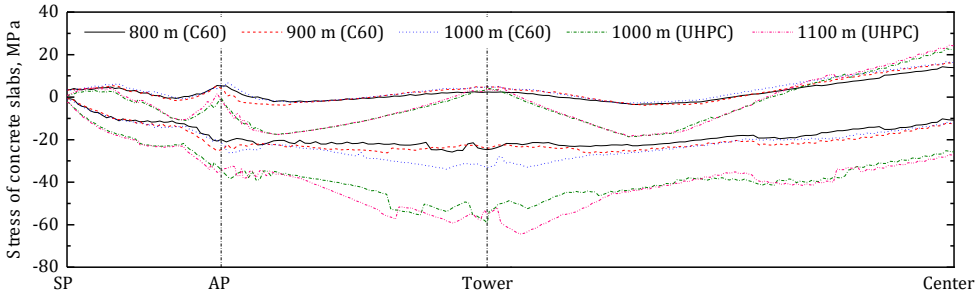

Figure 9. Longitudinal normal stress envelopes of concrete slabs

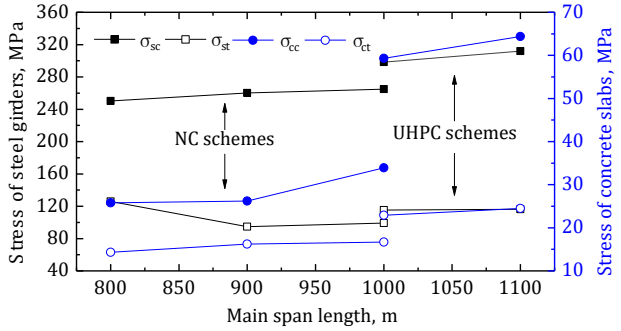

Figure 10. Variation of most unfavourable compressive and tensile stresses with main span length

The results in Figures 8 and 9 show that the unfavourable compressive stress of the steel girders mainly occurs in cross-sections near the bridge towers and auxiliary piers, while the maximum tensile stress occurs in the mid-span cross-section. The most unfavourable stress of steel girders is the compressive stress. The stress distribution characteristics of the concrete slabs are generally similar to those of the steel girders, i.e., the most unfavourable compressive and tensile stress appears in the cross-sections near the bridge tower and the mid-span section, respectively.

Figure 10 shows that the maximum compressive stress of steel girders and the most unfavourable compressive and tensile stresses of concrete slab increase as the main-span length increases. When the main span reaches 1000 m, the increase of the maximum compressive stress of the design scheme using NC-C60 concrete slab is even greater, which represents a potential restriction on the further growth of the main-span length for schemes using NC slabs. On the other hand, the use of UHPC leads to a considerable increase in the maximum compressive stress of the concrete slabs due to the significant reduction in the thickness of concrete slabs. However, the high strength of UHPC materials makes the stress response easier to meet material strength requirements, which will be discussed in the following sub-section.

3. Strength evaluation

To further assess the feasibility of each trial design scheme from the perspective of static strength, it is necessary to conduct strength evaluation. Firstly, the strength evaluation criteria for composite deck section need to be clarified. Considering that the plastic rotation capacity of a composite deck section is usually limited by the local buckling of the steel plates, the Chinese code for design of highway steel-concrete composite bridge (JTG/T D64-01–2015, 2015) stipulates that the load effect and the bearing capacity of composite deck sections should be calculated using the elastic and linear-elastic method, respectively, and the sign of reaching the bearing capacity of a composite deck section is that the stress at any point of the section reaches the design value of material strength. The stress response σ on any cross-sections should meet the following relation:

$$\gamma_0 \sigma \leq f, \tag{1}$$

where γ_0 is the factor for importance of structure and is 1.1 in this study, and f represents the design strength of reinforcing bars, steel plates or concrete. The stress response σ of the main girder can be obtained from the TDV RM Bridge program. Due to the difference between the linear-elastic composite section modelled in the FE program without modelling of the actual reinforcing bars and the actual composite section that has the contribution of the reinforcement and allows concrete cracking, the design strength f used for evaluation of the stress response

obtained from the FE model should be modified based on the assumption that the composite section in FE model and the actual composite section have the same combined bearing capacity of axial force and moment. The concept of equivalent design strength was thus proposed in this study to replace the theoretical design strength of different materials for strength evaluation. Figure 11 shows the simplified diagrams of various sections involved in the derivation of equivalent design strength. It should be explained that the I-shaped cross-section in the figure is only a simplified representation of the steel-concrete composite cross-section that consists of a composite deck system and double steel box girders.

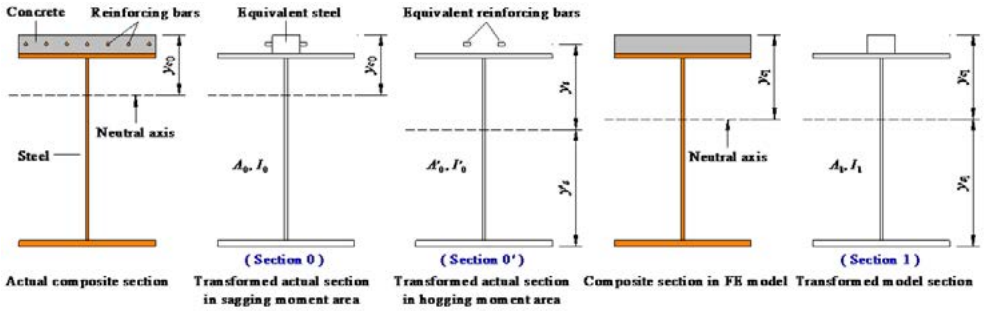

Figure 11. Simplified diagram of calculation models for composite cross-sections

For the compressive strength evaluation of concrete slabs in sagging moment areas, the design compressive strength of concrete was modified considering the influence of the reinforcement in concrete slabs. Based on the linear-elastic analysis principle and that the actual composite section and the linear-elastic composite section in FE model have the same combined bearing capacity composed of the ultimate axial compressive force N_{cu} and sagging moment M_u, the relationship between the equivalent compressive strength f_{cd_e} and the design strength f_{cd} of concrete can be given by

$$f_{cd\_e} = \left(\frac{N_{cu}}{A_1} + \frac{M_u y_{c1}}{I_1} \right) \frac{E_c}{E_s} = \eta_c f_{cd}, \tag{2}$$

$$f_{cd} = \left(\frac{N_{cu}}{A_0} + \frac{M_u y_{c0}}{I_0} \right) \frac{E_c}{E_s}, \tag{3}$$

$$\min\left(\frac{A_0}{A_1}, \frac{I_0 y_{c1}}{I_1 y_{c0}} \right) \le \eta_c \le \max\left(\frac{A_0}{A_1}, \frac{I_0 y_{c1}}{I_1 y_{c0}} \right), \tag{4}$$

where A and I respectively denote the area and moment of inertia of the transformed sections (see Figure 11) based on the conversion of material elastic modulus between concrete and steel; subscripts 0 and 1 represent the transformed section 0 and section 1, respectively; y_{c0} and y_{c1} are the vertical distance from the neutral axis of section 0 and section 1 to the top of the concrete slab, respectively; η_c is defined as the amplification factor of the design compressive strength and is related to the proportion between N_{cu} and M_u. Equation (4) gives the feasible range of η_c, which was derived from Equations (2) and (3).

For the tensile strength evaluation of concrete slabs in hogging moment areas, the design tensile strength of concrete was also modified to evaluate the stress response obtained from elastic analysis of the FE models, which has not considered the influence of reinforcement and concrete cracking on stress response. According to the provisions of the specification (JTG/T D64-01–2015, 2015), if the concrete cracking is considered, the contribution of concrete should not be taken into account in calculation of the flexural bearing capacity, but the effect of longitudinal reinforcing bars should be considered. Thus, the actual composite section in hogging moment areas was transformed to another equivalent steel section, i.e., section 0′ in Figure 11. According to the linear-elastic design principle, the combined bearing capacity of section 0′ composed of the ultimate axial compressive force N_{cu} and hogging moment M'_u corresponds to the critical yielding state of the reinforcing bars or the lower flange steel plate, as given by

$$f_{sd} = \frac{M'_u y_s}{I'_0} - \frac{N_{cu}}{A'_0}, \tag{5}$$

$$f'_d = \frac{M'_u y'_s}{I'_0} + \frac{N_{cu}}{A'_0}, \tag{6}$$

where A'_0 and I'_0 are the area and the moment of inertia of section 0′, respectively; y_s and y'_s represent the vertical distance from the neutral axis of section 0′ to the centre of the reinforcing bars and the bottom surface of the section, respectively. Through preliminary analysis, it was found that the ultimate load bearing state is usually controlled by the yielding of the lower flange steel plate, as described in Equation (6). Based on the same combined load bearing capacity of N_{cu} and M'_u between section 1 and section 0′, the equivalent tensile strength f_{td_e} of concrete can be expressed by

$$f_{td\_e} = \left(\frac{M'_u y_{c1}}{I_1} - \frac{N_{cu}}{A_1} \right) \frac{E_c}{E_s} = \left[\frac{M'_u y_{c1}}{I_1} - \frac{A'_0}{A_1} \left(f'_d - \frac{M'_u y'_s}{I'_0} \right) \right] \frac{E_c}{E_s} = \eta_t f_{td}, \tag{7}$$

where η_t is defined as the amplification factor of the design tensile strength of concrete, which depends upon the relative proportion between N_{cu} and M'_u. In the case of concrete slab in tension, the reinforcing bars in concrete slab are in tension as well when the lower flange steel plate yields, i.e.,

$$\frac{M'_{\mathrm{u}} y_{\mathrm{s}}}{I'_0} - \frac{N_{\mathrm{cu}}}{A'_0} \geq 0. \tag{8}$$

Based on Equations (6) and (8), the lower limit of M'_{u} can be obtained. On the other hand, it can be seen from Equation (6) that M'_{u} reaches the upper limit when N_{cu} is zero. Therefore, the ultimate hogging moment M'_{u} meets the following relation:

$$\frac{f'_{\mathrm{d}} I'_0}{y_{\mathrm{s}} + y'_{\mathrm{s}}} \leq M'_{\mathrm{u}} \leq \frac{f'_{\mathrm{d}} I'_0}{y'_{\mathrm{s}}}. \tag{9}$$

Accordingly, the range of the amplification factor η_{t} can be obtained by substituting Equation (9) into Equation (7), as given by

$$\left[\left(\frac{y_{\mathrm{c1}}}{I_1} + \frac{A'_0 y'_{\mathrm{s}}}{A_1 I'_0}\right)\frac{I'_0}{y_{\mathrm{s}} + y'_{\mathrm{s}}} - \frac{A'_0}{A_1}\right]\frac{E_{\mathrm{c}} f'_{\mathrm{d}}}{E_{\mathrm{s}} f_{\mathrm{td}}} \leq \eta_{\mathrm{t}} \leq \left[\left(\frac{y_{\mathrm{c1}}}{I_1} + \frac{A'_0 y'_{\mathrm{s}}}{A_1 I'_0}\right)\frac{I'_0}{y'_{\mathrm{s}}} - \frac{A'_0}{A_1}\right]\frac{E_{\mathrm{c}} f'_{\mathrm{d}}}{E_{\mathrm{s}} f_{\mathrm{td}}}. \tag{10}$$

For the strength evaluation of the steel components of the composite section, only the most unfavourable compressive stress under the combined action of axial compressive force and hogging moment was evaluated because that the main girder of a cable-stayed bridge bears enormous axial force and the steel material has the same tensile and compressive strength. The equivalent compressive strength $f'_{\mathrm{d\_e}}$ of steel material can be expressed as

$$f'_{\mathrm{d\_e}} = \frac{N_{\mathrm{cu}}}{A_1} + \frac{M'_{\mathrm{u}} y_{\mathrm{s1}}}{I_1} = \eta_{\mathrm{s}} f'_{\mathrm{d}}, \tag{11}$$

where N_{cu} and M'_{u} respectively represent the combined ultimate axial compressive force and hogging moment for section 0′ corresponding to the critical yielding state of the lower flange steel plate (see Equation (6)), y_{s1} is the vertical distance between the neutral axis and the bottom edge of section 1, and η_{s} is the amplification factor of the design compressive strength of steel. When considering the adverse impact of concrete cracking on the stress response of steel girders, the feasible range of η_{s} can be obtained by substituting Equations (6) and (9) into Equation (11), as given by

$$\left(\frac{y_{\mathrm{s1}}}{I_1} - \frac{y'_{\mathrm{s}} A'_0}{I'_0 A_1}\right)\frac{I'_0}{y_{\mathrm{s}} + y'_{\mathrm{s}}} + \frac{A'_0}{A_1} \leq \eta_{\mathrm{s}} \leq \left(\frac{y_{\mathrm{s1}}}{I_1} - \frac{y'_{\mathrm{s}} A'_0}{I'_0 A_1}\right)\frac{I'_0}{y'_{\mathrm{s}}} + \frac{A'_0}{A_1}. \tag{12}$$

However, when the tensile stress of concrete does not exceed the design tensile strength, the contribution of the concrete material in load bearing capacity can be taken into account. In this case, the design compressive strength f'_{d} of steel was directly used for simplicity to evaluate the stress response of steel girders obtained from the elastic FE model, without calculating $f'_{\mathrm{d\_e}}$ to consider the contribution of reinforcement in concrete slabs.

Based on the strength evaluation criteria stated in this study, the equivalent design strengths depend upon the design parameters of the composite deck section, including the geometric dimensions, reinforcement parameters and design

strength of materials. In this study, longitudinal reinforcing bars with a diameter of 22 mm and a reinforcement ratio of 2% were adopted for the NC slabs referring to the previous research on steel-NC composite deck (Su et al., 2018). For the UHPC slabs, longitudinal reinforcing bars with a diameter of 10 mm and a reinforcement ratio of 1.74% were selected based on the research of Liu et al. (2019). Based on the reinforcement parameters and the detailed design parameters shown in Tables 1 and 2, the structural parameters involved in Equations (2)–(12) can be calculated, and then the equivalent design strengths including $f_{\mathrm{cd\_e}}$, $f_{\mathrm{td\_e}}$ and $f'_{\mathrm{d\_e}}$ can be obtained. Considering that the main geometric dimensions of the main girders for different span schemes using the same concrete material are relatively similar, the equivalent design strengths of the trial design scheme with a main span of 1000 m were used as representatives for simplicity.

According to Equation (4), the amplification factor η_{c} of the design compressive strength for the NC slab is between 1.04 and 1.05. Considering that the maximum compressive stress of concrete slabs occurs near the bridge tower and is dominated by the axial force, therefore η_{c} is taken as 1.04. Similarly, η_{c} for the UHPC slab is 1.03. Since the maximum tensile stress of concrete slabs appears in the mid-span section where the axial force is zero, thus η_{t} is calculated to be 13.22 for the NC slab and 4.24 for the UHPC slab according to Equation (10).

The calculation of the equivalent design compressive strength $f'_{\mathrm{d\_e}}$ of steel mainly considers the adverse effects of concrete cracking. For design schemes with NC slabs, it can be seen from Figures 8 and 9 that the tensile stress of the concrete slab in cross-sections with unfavourable compressive stress of steel girders exceeds the design tensile strength of material, which means the occurrence of concrete cracking. Therefore, the design compressive strength of steel should be modified, and the range of the amplification factor η_{s} calculated based on Equation (12) is between 0.816 and 0.908, depending upon the proportion between N_{cu} and M'_{u}. Since the maximum compressive stress of steel girders appears near the auxiliary piers where the proportion between the axial force and hogging moment is medium, thus a compromise value of 0.862 is approximately adopted for η_{s}. For design schemes with UHPC slabs, the tensile stress of concrete slab in cross-sections with unfavourable compressive stress of steel girders is lower than the design tensile strength of UHPC, therefore the contribution of the concrete material in load bearing capacity can be considered and the design compressive strength of steel is directly used for strength evaluation.

Based on the amplification factors analysed above, the equivalent design strength of concrete slabs and steel girders were obtained. Table 3 provides a comparison between the maximum stress responses of different span schemes and corresponding equivalent design strengths. It can be seen that the stress responses of the 800 m and 900 m main span schemes with C60 concrete slabs can meet the strength requirements. When the main span reaches 1000 m, the maximum

compressive stress of the C60 concrete slab increases significantly and greatly exceeds the equivalent material strength, limiting the further growth of the main-span length. The use of UHPC with ultra-high material strength significantly reduces the thickness of concrete slabs, which makes the weight of the composite girder reduced by about 25%. In addition, although the maximum compressive stress of the concrete slab increases significantly when the thin UHPC slab is used, the safety margin remains large due to the high compressive strength of material, and the main static factor that limits the span growth turns to be the stress response of steel girders. When the main-span length reaches 1100 m, the maximum compressive stress of the steel girders slightly exceeds the design strength, basically meeting the design requirements.

Table 3. Comparison between the maximum stress response and corresponding equivalent design strength

Span, m	Concrete slab				Steel girder	
	σ_{cc}, MPa	f_{cd_e}, MPa	σ_{ct}, MPa	f_{td_e}, MPa	σ_{sc}, MPa	f'_{d_e}, MPa
800 (C60)	25.8	27.6	14.3	25.9	250.4	263
900 (C60)	26.2	27.6	16.2	25.9	260.1	263
1000 (C60)	*33.9*	*27.6*	16.7	25.9	*265.0*	*263*
1000 (UHPC)	59.3	100.6	22.9	33.9	298.4	305
1100 (UHPC)	64.4	100.6	24.5	33.9	311.9	305

2.4. Stiffness analysis

The stiffness analysis of bridges mainly focuses on the ratio of the vertical deflection of main girder to main-span length under the action of vehicle loads (JTG/T 3365-01–2020, 2020). The deflection envelope of the main girder under the vehicle load for each trial design scheme is shown in Figure 12(a). It can be seen that although the maximum deflection at mid-span becomes larger as the main-span length increases, the deflection-to-span ratio for each trial design scheme is far less than the limit value of 1/400 specified in relevant specification (JTG/T 3365-01–2020, 2020), indicating that the deflection response is not a dominant factor for the design of the long-span cable-stayed bridges involved in this study. In addition, the distribution of the lateral deflection of main girders under the action of transverse wind with a return period of 100 years was also analysed, as shown in Figure 12(b). Although there is no clear limit value for this lateral deflection in current Chinese specifications, it can be seen that the ratio of lateral deflection to span length is generally small for each trial design scheme.

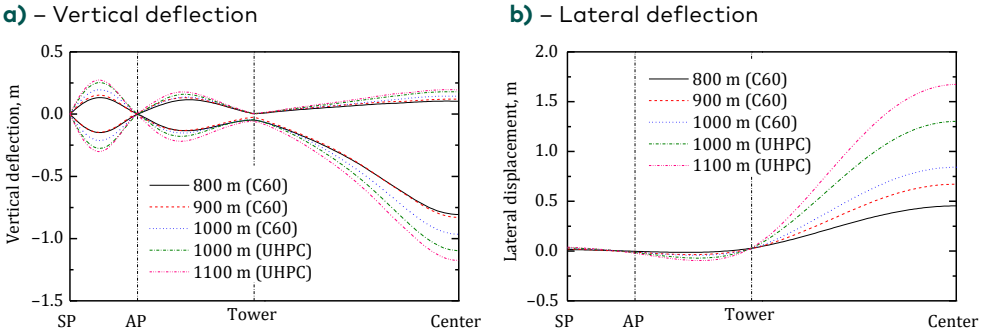

Figure 12. Deflection envelope of main girder

2.5. Static stability analysis

Static stability performance is an important concern for long-span cable-stayed bridges, and thus was analysed for the designed bridges. The analysis results indicate that the first instability mode of each trial design scheme occurs under the combined action of dead load, full-span live load and longitudinal operational wind load, and the instability mode is the in-plane buckling of the main girder. Table 4 shows the first instability mode and corresponding stability safety coefficient (φ) of each trial design scheme.

Table 4. First instability mode and stability safety coefficient

Span, m	φ	First instability mode	Variation of φ with span
800 (C60)	7.011		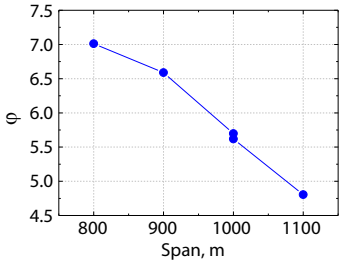
900 (C60)	6.588		
1000 (C60)	5.698		
1000 (UHPC)	5.619		
1100 (UHPC)	4.805		

It can be seen that the coefficient φ of each trial design scheme is greater than 4.0, meeting the requirements specified in the relevant specification (JTG/T 3365-01–2020, 2020), and an approximately linear decrease of φ with the increase of the main span-length can be observed.

3. Parametric analysis on structural static performance

To investigate the influence of main structural parameters on the static performance of the designed cable-stayed bridges, parametric analyses were conducted on the trial design schemes. Based on the parametric analysis results, the dominant structural parameters that affect different static effects were identified. Moreover, the feasible ranges of different structural parameters were obtained for each span scheme.

3.1. Parametric analysis conditions

The influence of the main structural parameters of main girders, including the height and width of main girder, thickness of the concrete slab and steel plate of composite deck, and thickness of the lower flange steel plate of steel girder, on key structural static performance was investigated. The structural static performance concerned in this study includes the maximum compressive stress of steel girders (σ_{sc}), the maximum tensile stress (σ_{ct}) and compressive stress (σ_{cc}) of concrete slabs, the mid-span vertical deflection (d_v) under vehicle loads, the mid-span transverse deflection (d_l) under extreme transverse static wind loads, and the static-stability safety coefficient (φ).

The parametric analysis conditions are summarised in Table 5. The height of main girders is changed by adjusting the web height of steel girders, while the thickness of concrete slab and the other steel plates remains unchanged. The variation of the main girder width is realized by adjusting the centre distance of the double box-shaped steel girders. The thickness variation values of the concrete slab and steel plate of the composite deck, as well as the lower flange steel plate, are kept the same along the bridge span. Meanwhile, the height of the main girder remains unchanged by simultaneously adjusting the web height. The benchmark of each parameter in Table 5 is the initial structural parameters described in Section 2.2 for each trial design scheme. The parametric analysis on static performance adopts the univariate method, which changes the individual structural parameters in Table 5 while keeping the remaining structural parameters unchanged. For each analysis case, the cable forces are re-optimised to achieve a reasonable finished state of bridge.

Table 5. Summary of parametric analysis cases

Parameter	Variation range		Interval
Main girder height H, m	δH	–1.5–0.5	0.5
Main girder width B, m	δB	–4–4	2
Thickness of concrete slab t_c, cm	δt_c	–2–2	1
Thickness of steel deck plate t_s, mm	δt_s	–4–4	2
Thickness of lower flange steel plate t_f, mm	δt_f	–10–10	5

3.2. Parametric analysis results

The static effects of different trial design schemes under different structural parameter conditions are shown in Figure 13. The thresholds for different static responses are also shown in this figure using dashed lines. Considering that the maximum vertical deflections (d_v) of different span schemes under different parameter conditions are far less than the limit values stipulated in the specification (JTG/T 3365-01–2020, 2020), and the maximum transverse deflections (d_l) are generally moderate and have not been explicitly limited in relevant specifications, thus the parametric analysis results for d_v and d_l are not given in Figure 13.

The results in Figure 13 indicate that the influence of structural parameters on relevant static performance is generally similar between different span schemes. The maximum compressive stress of steel girders is most affected by the main girder height H and the thickness of the lower flange steel plate t_f, and this stress can be effectively reduced by raising H or t_f. The maximum tensile and compressive stresses of concrete slabs are most sensitive to the main girder width B, especially when the span length becomes larger. The main reason is that the transverse bending moment caused by the cross-wind load increases nonlinearly with the increase of the main-span length, thus the proportion of the stress caused by the transverse bending moment in the total stress increases accordingly, and this stress is closely related to the value of B. The static-stability safety coefficient is mainly affected by the main girder height, and increases rapidly as H increases. Additionally, moderate changes in thickness of the concrete slab and steel deck plate of the composite deck have relatively small influence on the overall mechanical performance of the main girder, and they may have greater impacts on the local mechanical performance of the composite deck system.

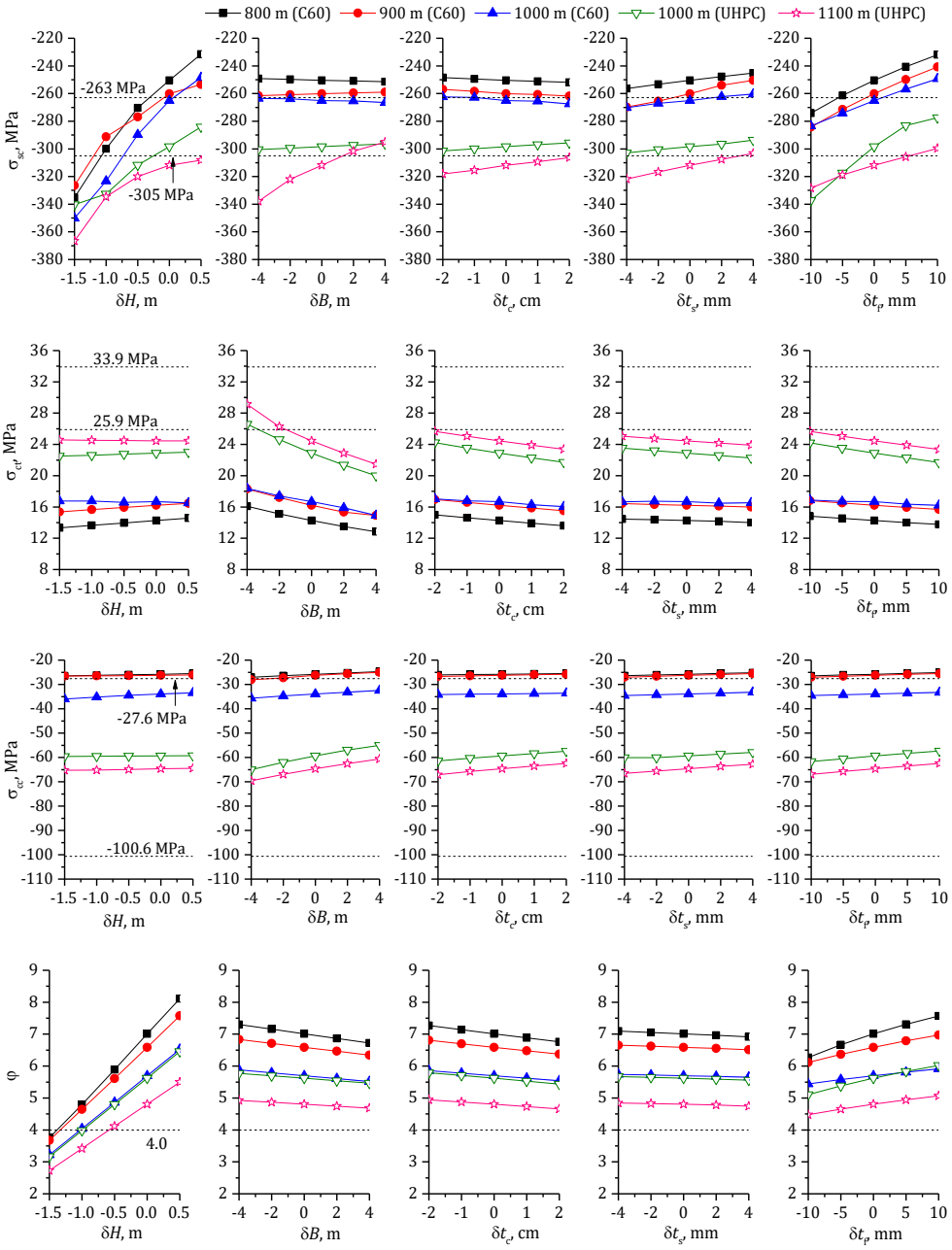

Figure 13. Static performances under different structural parameters

According to the parametric analysis results and response thresholds shown in Figure 13, the feasible ranges for different structural parameters, which are within the parameter ranges concerned in this study, were further calculated by linear interpolation, as shown in Table 6. It is worth noting that the feasible ranges were obtained based on univariate method, therefore the combination of various structural parameters in these feasible ranges does not necessarily mean the static feasibility of the corresponding bridge scheme.

Table 6. Feasible ranges for main structural parameters

Parameter / Span, m	*H*, m	*B*, m	δt_c, cm	t_s, mm	δt_f, mm
800 (C60)	>3.68	≥35.5	≥–2.0	≥4.0	≥–5.0
900 (C60)	>3.91	>36.6	≥–2.0	≥7.0	≥–1.0
1000 (C60)	None	None	None	None	None
1000 (UHPC)	>3.75	≥35.5	≥–2.0	≥4.0	≥–1.0
1100 (UHPC)	None	>40.8	None	≥12.0	≥6.0

Notes: "None" indicates that there is no relevant parameter range that meets the static requirements.

4. Variation of static performance with span length

Based on the static analysis results of different span schemes with different structural parameters, the variations of dominant static effects with main span length were obtained, as shown in Figure 14. The static effects in this figure are the optimised results based on parametric analysis. For the NC-slab schemes, the main static factor controlling the structural design is the compressive stress of concrete slabs (σ_{cc}) (see Table 3). It can be seen from Figure 13 that the main structural parameters concerned in this study have little influence on σ_{cc}. Therefore, the static performance of the initial NC-slab schemes was employed. For the UHPC-slab schemes, the determinative static factor is the compressive stress of steel girders (σ_{sc}) (see Table 3), while the main structural factors affecting σ_{sc} include the main girder height and the thickness of the lower flange steel plate. Considering that the main girder height of 4 m in the initial design schemes is relatively high, thus it was kept unchanged and only the thickness of the lower flange steel plate was increased to reduce σ_{sc}. The maximum thickness of the lower flange steel plate of the UHPC-slab schemes with main-span lengths of 1000 m and 1100 m was increased to 63 mm, which is the upper limit for the thickness of steel plates corresponding to the design strength of 305 MPa used in this study, as specified in the specification (JTG

D64–2015, 2015). Then the optimised static responses of the UHPC-slab schemes were obtained by linear extrapolation of relevant parametric analysis results.

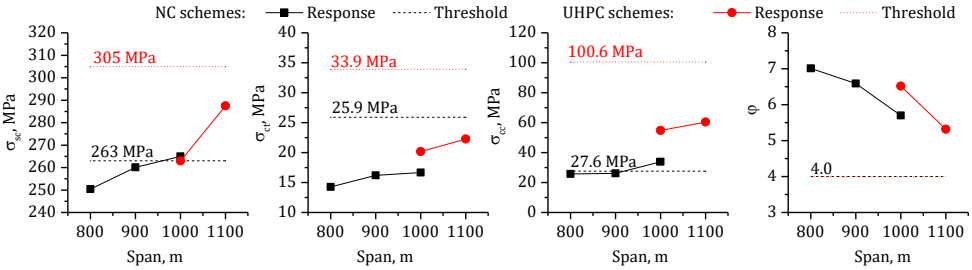

Figure 14. Variation of static response with main-span length

It can be seen from Figure 14 that the dominant stress response after optimisation increase and the static stability coefficient decreases as the span increases. The static performance of NC-slab schemes with main spans of 800 m and 900 m can meet the static requirements. When the main span reaches 1000 m, the maximum compressive stress of the concrete slab greatly exceeds the concrete strength, limiting the further growth of the main-span length. The optimised UHPC-slab schemes with main spans of 1000 m and 1100 m can meet the static design requirements, with the unfavourable static effects being the compressive stress of steel girders and the static-stability safety coefficient, which have relatively small safety margins.

The linear interpolation or extrapolation of the main-span length with respect to the static responses shown in Figure 14 was further conducted to explore the room for further increasing the span of OCCBs with SCD under the overall layout parameter conditions (e.g., the side-to-main span ratio and tower height-to-span ratio) assumed in the present study and the optimal main girder parameter conditions obtained by the parametric analysis. The interpolation results show that when the main span of the NC and UHPC schemes reaches approximately 920 m and 1170 m, respectively, the maximum compressive stress of the concrete slab and the steel girder reaches corresponding allowable strength value. A span growth rate of approximately 25% was observed using the UHPC slabs instead of the NC slabs, which is close to the reduction rate of the dead-weight of the composite girder. Additionally, according to the parametric analysis results, appropriate increase in main girder height can to some extent further expand the applicable span of the cable-stayed bridges concerned in this study.

Conclusion

Trial design schemes of long-span OCCBs with SCD were proposed. The mechanical performance and static feasibility of the design schemes, the influence of different structural parameters on key static responses, and the variation of static effects with main span length were investigated, and the following conclusions were summarised.

(1) The main static responses of the NC-slab schemes with main spans of 800 m and 900 m and the UHPC-slab schemes with main spans of 1000 m and 1100 m can meet the requirements of static strength, stiffness and stability. The NC-slab scheme with a main span of 1000 m has a large dead weight, making the compressive stress of the concrete slab exceed the allowable strength value, and thus limiting the further growth of span length. The use of UHPC greatly improves the compressive strength of the concrete slab and effectively reduces the dead weight of the main girder by approximately 25%, which makes the proposed kilometre-level UHPC-slab schemes meet the requirements of static strength, and the most unfavourable static effect turns to be the maximum compressive stress of steel girders.

(2) Under the assumed overall layout parameter conditions, parametric analysis results for the key structural parameters of the main girder indicate that the compressive stress of steel girders of the composite girder can be most effectively reduced by raising the main girder height or thickness of the lower flange steel plate, while the tensile and compressive stresses of the concrete slab are most sensitive to the main girder width, especially when the span length becomes larger. The static-stability safety coefficient is most affected by the main girder height. Moderate changes in thickness of the concrete slab and steel deck plate of the composite deck system generally have small influence on the overall static performance of the main girder. The parametric analysis results provide a series of static feasible solutions for composite girder cable-stayed bridges with main spans not exceeding 1100 m.

(3) The interpolation results based on the parametric analysis achievements show that under the overall layout parameter conditions (e.g., the side-to-main span ratio and tower height-to-span ratio) assumed in the present study, when the main span of the NC and UHPC schemes reaches approximately 920 m and 1170 m, respectively, certain dominant static effect reaches corresponding allowable value. Using UHPC for the composite deck section instead of NC improves the spanning capacity of cable-stayed bridges by approximately 25%, close to the reduction rate of the dead-weight of main girder. Appropriately increasing the main girder height, optimising the side-to-main span ratio and tower height-to-span ratio, etc., may probably further expand the applicable span of OCCBs with SCD, which is expected to be investigated in future research work.

Acknowledgements

The authors gratefully acknowledge the support of the National Natural Science Foundation of China and Shanghai Frontiers Science Centre of "Full Penetration" Far-Reaching Offshore Ocean Energy and Power.

Funding

This work was supported by the National Natural Science Foundation of China under Grant number 52008240.

Author Contributions

Tingting MA conceived the study. Tingting MA and Shishou ZHANG were responsible for the design and development of the data analysis. Shishou ZHANG and Meitao SHANG were responsible for data collection and analysis. Tingting MA and Shishou ZHANG were responsible for data interpretation. Tingting MA wrote the first draft of the article.

Disclosure Statement

The authors have no conflicts of interest to declare.

Statement of the Use of Generative AI and AI-assisted Technologies in the Writing Process

In the preparation of this manuscript, no AI technologies were used for text generation, data interpretation, figure creation, reference recommendation, or any other aspect of the research or writing process. All scientific content, data analysis, and conclusions are entirely the original work of the authors.

REFERENCES

Al-Ramahee, M. A., Chan, T., Mackie, K. R., Ghasemi, S., & Mirmiran, A. (2017). Lightweight UHPC-FRP composite deck system. *Journal of Bridge Engineering*, *22*(7), Article 04017022. https://doi.org/10.1061/(ASCE)BE.1943-5592.0001049

Arellano, H., Gomez, R., & Tolentino, D. (2019). Parametric analysis of multi-span cable-stayed bridges under alternate loads. *The Baltic Journal of Road and Bridge Engineering*, *14*(4), 543–567. https://doi.org/10.7250/bjrbe.2019-14.457

Chen, S., Huang, Y., Gu, P., & Wang, J. Y. (2019). Experimental study on fatigue performance of UHPC-orthotropic steel composite deck. *Thin-Walled Structures*, *142*, 1–18. https://doi.org/10.1016/j.tws.2019.05.001

Jiao, C. Y., Wang, H. B., Yan, B., Wei, B., Hu, Z. L., Zheng, X. L., Fang, R., & Wu, R. R. (2024). Impact of the structural system type on the seismic fragility of a multi-tower cable-stayed bridge. *Structure and Infrastructure Engineering*, 1–15. https://doi.org/10.1080/15732479.2024.2424908

Kim, H. Y., & Jeong, Y. J. (2010). Ultimate strength of a steel-concrete composite bridge deck slab with profiled sheeting. *Engineering Structures*, *32*(2), 534–546. https://doi.org/10.1016/j.engstruct.2009.10.014

Kim, T. W., Baek, J., Lee, H. J., & Lee, S. Y. (2014). Effect of pavement design parameters on the behaviour of orthotropic steel bridge deck pavements under traffic loading. *International Journal of Pavement Engineering*, *15*(5), 471–482. http://dx.doi.org/10.1080/10298436.2013.839790

Li, C., Ge, H., & Zhou, X. H. (2022). The Dongting lake bridge for an expressway in China: Design, construction and analysis. *Structural Engineering International*, *32*(3), 291–297. https://doi.org/10.1080/10168664.2020.1747371

Liao, Y., Ding, W. X., Liu, Y. Q., & Zhang, Y. J. (2023). Danjiangkou reservoir bridge, China: a new record for earth-anchored cable-stayed bridges. *Proceedings of the Institution of Civil Engineers-Civil Engineering*, *176*(1), 18–23. https://doi.org/10.1680/jcien.21.00237

Liu, Y. M., Zhang, Q. H., Meng, W. N., Bao, Y., & Bu, Y. Z. (2019). Transverse fatigue behaviour of steel-UHPC composite deck with large-size U-ribs. *Engineering Structures*, 180, 388–399. https://doi.org/10.1016/j.engstruct.2018.11.057

Martin, L. A., Yousif, Z., Campbell, B. L., Furrer, M., & Chynoweth, M. (2023). Planning and design of the Gordie Howe International Bridge, North America. *Proceedings of the Institution of Civil Engineers – Bridge Engineering*, *176*(4), 233–249. https://doi.org/10.1680/jbren.21.00057

Ministry of Transport of the People's Republic of China. (2018). *JTG 3362—2018: Specifications for Design of Highway Reinforced Concrete and Prestressed Concrete Bridges and Culverts* (In Chinese).

Ministry of Transport of the People's Republic of China. (2015). *JTG D64—2015: Specifications for Design of Highway Steel Bridge* (In Chinese).

Ministry of Transport of the People's Republic of China. (2018). *JTG/T 3360-01—2018: Wind-resistant Design Specification for Highway Bridges* (In Chinese).

Ministry of Transport of the People's Republic of China. (2020). *JTG/T 3365-01—2020, Specifications for Design of Highway Cable-stayed Bridge* (In Chinese).

Ministry of Transport of the People's Republic of China. (2015). *JTG/T D64-01—2015, Specifications for Design and Construction of Highway Steel-concrete Composite Bridge* (In Chinese).

Nagai, M., Fujino, Y., Yamaguchi, H., & Iwasaki, E. (2004). Feasibility of a 1,400 m span steel cable-stayed bridge. *Journal of Bridge Engineering*, *9*(5), 444–452. https://doi.org/10.1061/(ASCE)1084-0702(2004)9:5(444)

Shao, C. Y., Yan, H., Chen, L., Xu, Y., & Cao, S. L. (2019). Widening and strengthening of the Songpu Bridge. *Structural Engineering International*, *29*(3), 354–361. https://doi.org/10.1080/10168664.2019.1601052

Shao, X. D., & Cao, J. H. (2018). Fatigue assessment of steel-UHPC lightweight composite deck based on multiscale FE analysis: case study. *Journal of Bridge Engineering*, *23*(1), Article 05017015. https://doi.org/10.1061/(asce)be.1943-5592.0001146

Shao, X. D., Qu, W. T., Cao, J. H., & Yao, Y. L. (2018). Static and fatigue properties of the steel-UHPC lightweight composite bridge deck with large U ribs. *Journal of Constructional Steel Research*, *148*, 491–507. https://doi.org/10.1016/j.jcsr.2018.05.011

Shao, X. D., Yi, D. T., Huang, Z. Y., Zhao, H., Chen, B., & Liu, M. L. (2013). Basic performance of the composite deck system composed of orthotropic steel deck and ultrathin RPC Layer. *Journal of Bridge Engineering*, *18*(5), 417–428. https://doi.org/10.1061/(asce)be.1943-5592.0000348

Shao, X. D., Zhao, X. D., Liu, Q., Deng, S. W., & Wang, Y. (2022). Design and experimental study of hot rolled shape steel-ultrahigh performance concrete composite beam. *Engineering Structures*, *252*, Article 113612. https://doi.org/10.1016/j.engstruct.2021.113612

Su, Q. T., Dai, C. Y., & Jiang, X. (2019). Bending performance of composite bridge deck with T-shaped ribs. *Frontiers of Structural and Civil Engineering*, *13*(4), 990–997. https://doi.org/10.1007/s11709-019-0532-8

Su, Q. T., Dai, C. Y., & Xu, C. (2018). Full-scale experimental study on the negative flexural behavior of orthotropic steel-concrete composite bridge deck. *Journal of Bridge Engineering*, *23*(12), Article 04018097. https://doi.org/10.1061/(ASCE)BE.1943-5592.0001320

Syrkov, A. V., & Krutikov, O. V. (2014). Lifecycle optimization for Vladivostok-Russky isle bridge by means of risk analysis and monitoring. *Automation and Remote Control*, *75*(12), 2217–2224. https://doi.org/10.1134/s000511791412011x

Walter, R., Olesen, J. F., Stang, H., & Vejrum, T. (2007). Analysis of an orthotropic deck stiffened with a cement-based overlay. *Journal of Bridge Engineering*, *12*(3), 350–363. https://doi.org/10.1061/(ASCE)1084-0702(2007)12:3(350)

Wang, Z. M., Zhang, N., & Cheng, Q. (2023). Multi-objective optimization-based reasonable finished state in long-span cable-stayed bridge considering counterweights. *Structures*, *51*, 1497–1506. https://doi.org/10.1016/j.istruc.2023.03.061

Wen, Y., & Zhou, Z. W. (2022). Qualification of the Ernst formula for modeling the sag effect of super-long stay cables in the long-span railway cable-stayed bridges. *Structures*, *45*, 99–109. https://doi.org/10.1016/j.istruc.2022.09.002

Wolchuk, R. (1990). Lessons from weld cracks in orthotropic decks on three European bridges. *Journal of Structural Engineering*, *ASCE*, *116*(1), 75–84. https://doi.org/10.1061/(asce)0733-9445(1990)116:1(75)

Xiao, R. C., Jia, L. J., Song, X., & Xiang, H. F. (2001). Influence matrix method of cable tension optimization for long-span cable-stayed bridges. *IABSE Conference: Cable-Supported Bridges – Challenging Technical Limits*, Seoul, South Korea, 1–5. https://doi.org/10.2749/222137801796350013

Yang, X.Y., Gong, J.X., Wang, Y.H., Xu, B.H., & Zhu, J.C. (2017). Probability model and reliability analysis of cable stress for cable-stayed bridge. *The Baltic Journal of Road and Bridge Engineering*, *12*(4), 248–257. https://doi.org/10.3846/bjrbe.2017.31

Yang, Y. Q., Wang, X., & Wu, Z. S. (2020). Long-span cable-stayed bridge with hybrid arrangement of FRP cables. *Composite Structures*, *237*, Article 111966. https://doi.org/10.1016/j.compstruct.2020.111966

Yao, Y. L., & Shao, X. D. (2018). Economic and mechanical properties of large span cable-stayed bridges with lightweight steel-UHPC composite beam. *Highway Engineering*, *43*(1), 20–24 (In Chinese).

Zhang, X. J., Ni, B. B., & Zhao, T. J. (2024). Study on wind stability and favorable structural scheme of a three-tower cable-stayed bridge. *Wind and Structures, 39*(5), 367–380. https://doi.org/10.12989/was.2024.39.5.367

Zhao, X. W., Xiao, R. C., & Sun, B. (2019). Span limit and parametric analysis of cable-stayed bridges. *Structural Engineering and Mechanics*, *71*(3), 271–282. https://doi.org/10.12989/sem.2019.71.3.271